Diffraction effects on light-atomic-ensemble quantum interface

J. H. Muller, Plamen G. Petrov, Daniel Oblak, Carlos L. Garrido Alzar, Sr de Echaniz, Eugene S. Polzik

Diffraction effects on light–atomic-ensemble quantum interface

J. H. Müller,[1,*] P. Petrov,[1] D. Oblak,[1,2] C. L. Garrido Alzar,[1] S. R. de Echaniz,[3] and E. S. Polzik[1,†]
[1]*QUANTOP, Niels Bohr Institute, Copenhagen University, Blegdamsvej 17, DK-2100 København, Denmark*
[2]*Institute of Physics and Astronomy, University of Aarhus, Ny Munkegade Bldg. 520, DK-8000 Aarhus, Denmark*
[3]*ICFO-Institut de Ciències Fotòniques, Jordi Girona 29, Nexus II, E-08034 Barcelona, Spain*
(Received 19 April 2004; published 7 March 2005)

We present a simple method to include the effects of diffraction into the description of a light-atomic ensemble quantum interface in the context of collective variables. Carrying out a scattering calculation we single out the purely geometrical effect and apply our method to the experimental relevant case of Gaussian-shaped atomic samples stored in single beam optical dipole traps probed by a Gaussian beam. We derive simple scaling relations for the effect of the interaction geometry and compare our findings to the results from one-dimensional models of light propagation.

DOI: 10.1103/PhysRevA.71.033803 PACS number(s): 42.50.Ct, 42.25.Fx, 32.80.Qk

I. INTRODUCTION

Coupling collective variables of atomic ensembles to propagating modes of the electromagnetic field has been identified as an efficient tool to engineer the states of atoms and light at the quantum level. Several proposals for spin squeezing, mapping of quantum states between light and atoms, i.e., quantum memory operations, creation of macroscopic entanglement, and teleportation of atomic states have been published [1–8]. A number of these proposals have actually been verified experimentally using atomic samples stored in vapor cells as well as in magneto-optical traps [9–12]. The efficiency of the coupling is often discussed resorting to effective one-dimensional (1D) models for the light propagating through a homogeneous sample and the optical depth is found to be the essential parameter determining the coupling strength. This naturally suggests the use of cold and trapped atomic samples, where long coherence times for collective variables are possible, with a shape mimicking a 1D string of atoms to maximize column density for a given number of atoms. However, while the effective 1D models work well for wide and nearly homogeneous samples the question of light diffraction from small, inherently inhomogeneous samples and its impact on coupling efficiency immediately arises when cold and trapped atomic samples are used [13]. In a recent work [14], aspects of spatial inhomogeneity have been addressed via the introduction of different asymmetric collective variables.

The purpose of the present paper is twofold. We present a simple and effective semianalytic method to identify the spatial light mode that the atomic sample couples to, to quantify the strength of the coupling, and we use this method to find optimum shapes for atomic samples. In addition we derive simple scaling parameters describing the effect of the shape of the atomic sample which allow us to make a direct comparison with the established 1D quantum models and quantify the effect of diffraction on the coupling strength. Albeit we are ultimately interested in measuring and manipulating quantum states, we find it instructive to solve the underlying classical scattering problem first to single out the purely geometric effects, and we try to avoid hiding useful practical information behind the much more intricate mathematical formalism needed to solve the full quantum problem. Our approach delivers valuable information for designing experimental configurations, provides intuitive pictures, and may serve as a starting point for a more elaborate quantum theoretical treatment.

The remainder of the paper is organized as follows. In Sec. II we present briefly the main results of a quantum description of two modes of light coupled coherently to atoms in terms of collective variables and introduce typical experimental configurations. With the quantum model we derive an expression for the achievable signal-to-noise ratio when measuring collective atomic variables. After doing so we analyze the experimental configurations again in semiclassical terms and use this framework to point out the coherently scattered power by the atomic sample as the relevant quantity to optimize for good quantum coupling. Section III presents our model for calculating the scattering mode and the scattering efficiency of the atomic sample for different geometries together with some remarks on the assumptions made and the range of validity of the model. In Sec. IV we apply this model to atoms stored in a single beam optical dipole trap. In Sec. V we provide a comparison between our classical calculation and the results from effective 1D models. Section VI summarizes our results and points out possible extensions of our model.

II. COLLECTIVE LIGHT-ATOM COUPLING

The Hermitian part of the interaction of a pulse of off-resonant light with an ensemble of atoms with two ground states residing in a container with cross-sectional area A and length L can be described by an effective Hamiltonian of the form (see, e.g., Refs. [7,15–17])

$$\hat{H}_c = \hbar \frac{2\sigma_0}{A}\left(\frac{\Gamma}{2\Delta}\right)\int_0^L \hat{s}_z(z,t)\hat{j}_z(z,t)dz. \tag{1}$$

The factor in front of the integral describing the strength of the coupling of the collective variables contains the single-

*Electronic address: muller@nbi.dk
†URL: http://quantop.nbi.dk/index.html

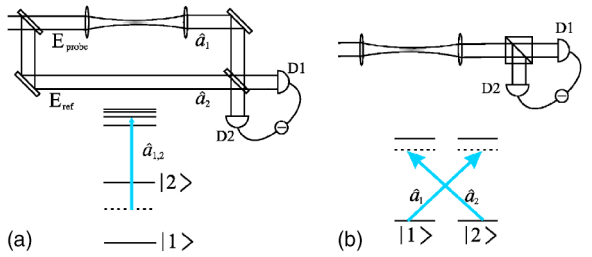

FIG. 1. (Color online) Mach-Zehnder and polarization interferometry setups for quantum coupling of collective variables of cold atomic samples to light. The local interaction energy is proportional to $\hat{a}_1^\dagger\hat{a}_1(|2\rangle\langle 2|-|1\rangle\langle 1|)$ in (a) and to $\hat{a}_1^\dagger\hat{a}_1|1\rangle\langle 1|+\hat{a}_2^\dagger\hat{a}_2|2\rangle\langle 2|$ in (b).

atom reactive response to radiation characterized by the resonant cross section σ_0, the detuning Δ in units of the natural linewidth Γ, and the cross-sectional area of the light mode governing the electric-field strength per photon occupying the mode. In Eq. (1) operators for the photon flux of light $\hat{\mathbf{s}}$ and ground-state polarization of atoms $\hat{\mathbf{j}}$ are introduced. For light we can write $\hat{\mathbf{s}}$ in terms of continuous mode creation and annihilation operators with boson commutation rules: $\hat{s}_x=\frac{1}{2}(\hat{a}_2^\dagger\hat{a}_1+\hat{a}_1^\dagger\hat{a}_2)$, $\hat{s}_y=\frac{1}{2i}(\hat{a}_2^\dagger\hat{a}_1-\hat{a}_1^\dagger\hat{a}_2)$, $\hat{s}_z=\frac{1}{2}(\hat{a}_2^\dagger\hat{a}_2-\hat{a}_1^\dagger\hat{a}_1)$. For simplicity of notation the time and spatial dependence of the operators has been suppressed. The mode index can specify for instance two fields propagating in the two legs of a Mach-Zehnder interferometer [Fig. 1(a)] or left and right circular polarized modes of a single laser beam [Fig. 1(b)]. The operators $\hat{\mathbf{s}}$ are normalized to describe the photon flux through a cross section of the light beams at location z along their path of propagation [18]. Integrating the photon fluxes over the duration of a pulse we can define dimensionless collective operators $\hat{\mathbf{S}}$ to describe a pulse as one entity. By construction the collective operators follow the usual commutator algebra for vector operators.

In the case of atoms we restrict ourselves, for simplicity, to the case of two ground states only. We define in analogy:

$$\hat{j}_x = (1/\delta z)\sum_{l=1}^{N_{at}(z)} \tfrac{1}{2}(|2\rangle_l\langle 1| + |1\rangle_l\langle 2|),$$

$$\hat{j}_y = (1/\delta z)\sum_{l=1}^{N_{at}(z)} (1/2i)(|2\rangle_l\langle 1| - |1\rangle_l\langle 2|),$$

$$\hat{j}_z = (1/\delta z)\sum_{l=1}^{N_{at}(z)} \tfrac{1}{2}(|2\rangle_l\langle 2| - |1\rangle_l\langle 1|),$$

where the sum extends over the number of atoms $N_{at}(z)$ residing in a thin slice of the interaction volume at position z [19]. A continuum limit is taken by shrinking the thickness δz of the slices to zero. The three operators $\hat{j}_i$ describe the coarse grained linear density of Bloch-vector components for the two-level system formed by the two ground states. Again we can choose to describe the atomic sample as a whole by integrating over the length of the atomic sample defining collective atomic operators $\hat{\mathbf{J}}$.

Inherent in this description are the assumptions that the transverse-mode function of the light field is a frozen variable, hence the 1D integration over the Hamilton density in Eq. (1), and that the atoms scatter light coherently only into the input modes. This is a good approximation for atomic ensembles and light fields transversally much wider than an optical wavelength and not too long samples. In addition, since the operator nature of atomic position is suppressed, the spatial density distribution of the atoms is not changed by the interaction with the radiation in this model.

The dynamics generated by Eq. (1) at the level of expectation values describes differential phase shifts of the light modes due to coherent forward scattering by the atoms in the two ground states and differential shifts of the atomic energy levels due to the intensity difference of the two light modes. This dynamics can be conveniently visualized with the help of coupled Bloch spheres for light and atom variables. Of particular interest for practical quantum state engineering is the case of initial conditions with $\hat{J}_x^{in}$ and $\hat{S}_x^{in}$ large and classical, i.e., uncorrelated coherent states with expectation values on the order of half the total number of atoms and photons, respectively. In this case the dynamical evolution of the system is driven entirely by the fluctuations of light and atomic variables. In the experimental setup sketched in Fig. 1(b) this corresponds to linearly polarized input light and all atoms in a balanced coherent superposition of the two ground states, such that there is a macroscopic magnetic polarization in the plane orthogonal to the direction of propagation. For the setup advertised in Fig. 1(a) this amounts to a balanced coherent superposition of atomic levels 1 and 2 and 50-50 beam splitters at entrance and exit of the Mach-Zehnder interferometer. Linearizing the spectrum of the operators around their expectation values and integrating the dynamics, to leading order, input-output relations can be written for the fluctuations of the collective operators orthogonal to the coherent excitation [20,21]:

$$\delta\hat{J}_y^{out} = \delta\hat{J}_y^{in} - \frac{2\sigma_0}{A}\frac{\Gamma}{2\Delta}\langle\hat{J}_x\rangle\delta\hat{S}_z^{in},$$

$$\delta\hat{J}_z^{out} = \delta\hat{J}_z^{in},$$

$$\delta\hat{S}_y^{out} = \delta\hat{S}_y^{in} - \frac{2\sigma_0}{A}\frac{\Gamma}{2\Delta}\langle\hat{S}_x\rangle\delta\hat{J}_z^{in},$$

$$\delta\hat{S}_z^{out} = \delta\hat{S}_z^{in}.$$

The superscript *in* (*out*) refers for atomic variables to times before (after) passage of the pulse through the sample and for light variables to observation planes in front of (behind) the sample. From these relations we can calculate the variance of a set of measurements on identically prepared systems. A set of measurement records of $\hat{S}_y^{out}$ will show a mean value $\langle\hat{S}_y^{out}\rangle=0$ and a variance:

$$\mathrm{Var}(\hat{S}_y^{out}) = \frac{n_{ph}}{4} + \left(\frac{2\sigma_0}{A}\frac{\Gamma}{2\Delta}\frac{n_{ph}}{2}\right)^2\frac{N_a}{4}.$$

Here the first term on the right-hand side reflects the noise of the coherent input state of light, with n_{ph} the total number of photons in a pulse, while the second term describes the excess fluctuations imprinted onto the light by the fluctuations

of the atomic variable $\hat{J}_z^{in}$ and amplified by the large coherent amplitude of S_x. From the measurement record we can infer a value for the atomic variable $\hat{J}_z^{in}$, i.e., the population difference with a confidence interval limited by the first term, i.e., with a signal-to-noise ratio (S/N) of

$$\left(\frac{S}{N}\right)_{1D}^2 = \frac{\sigma_0^2}{A^2} N_{at} n_{ph} \left(\frac{\Gamma}{2\Delta}\right)^2. \tag{2}$$

Projection of the atomic state by the destructive measurement on light, will leave the collective atomic variable $\hat{J}_z^{in}$ in a state with fluctuations reduced below the standard quantum limit if the signal-to-noise ratio is finite and if added noise due to spontaneous emission is small enough [22]. In practical terms this means that repeated measurements on the same atomic system will show a covariance below the projection noise [23]. To the extent the measurement is nondestructive, this fact can be exploited to write, store, and retrieve quantum information to and from the atomic variable [12,24]. Instead of measuring destructively the light pulse after a single pass through the atomic ensemble one can allow for multiple interaction together with appropriate switching of the coupling Hamiltonian between consecutive passes. This way unconditional quantum state preparation is possible and the measurement serves merely as a verification of successful state preparation [8,22,25]. In this more general setting the above defined signal-to-noise ratio plays the role of a coupling strength κ^2:

$$\kappa^2 = \frac{\sigma_0^2}{A^2} N_{at} n_{ph} \left(\frac{\Gamma}{2\Delta}\right)^2 = \alpha_0 \eta \tag{3}$$

which can be conveniently expressed as the product of integrated spontaneous emission rate $\eta = n_{ph}(\sigma_0/A)(\Gamma/2\Delta)^2$ and the optical depth or column density $\alpha_0 = N_{at}(\sigma_0/A)$, explaining the use of the optical depth as a figure of merit for collective variable light-atom coupling [25]. The interaction geometry, of course, stays the same, so diffraction of light discussed in the following has the same impact on the coupling strength in these schemes.

After this brief review of the 1D quantum model, we look again at the experimental configuration in Fig. 1(a) [26], seeking this time a description in purely classical terms and pointing out where we go beyond the 1D model. A cloud of cold atoms residing in one arm of the interferometer is loaded into a far-off-resonant dipole trap created by a focused Gaussian beam. Probe light with a wave vector $k = 2\pi/\lambda$ enters the interferometer from the left and passes through the atomic sample. The light experiences a phase shift caused by the refractive index of the sample, which is determined by both the atomic density distribution and by the population difference of the two sublevels $\delta N_{at} = N_2 - N_1$. For simplicity we assume here equal strength of the transitions connecting the two ground states to the excited states and equal and opposite detuning as indicated in Fig. 1(a). Given an atomic density distribution the light carries thus information about the level populations after passage through the sample. In turn, the atomic energy levels are shifted differentially during the interaction and thus information about the light is deposited in the coherence between the atomic levels. To assess the sensitivity of a measurement of the atomic population difference we look at the signal by the balanced homodyne detector (with quantum efficiency ε) on the right upon detection of a pulse of light (frequency ω) of duration τ. The detector signal S_D, i.e., the photocurrent i_s in units of the elementary charge e integrated over the pulse duration, in the presence of atoms is given by

$$S_D = \int_0^\tau \frac{i_s}{e} dt = \varepsilon \frac{\tau}{\hbar\omega} \frac{c\varepsilon_0}{2} \left(2|E_{sc}||E_{ref}| \int_{A_D} M_{sc} M_{ref} dA + 2|E_{probe}||E_{ref}| \int_{A_D} M_{probe} M_{ref} dA \right). \tag{4}$$

Here E_{probe} (E_{ref}) denotes the initial field in the probe (reference) arm. The integrals over the detector area describe the overlap of the transverse mode functions $M_{sc}, M_{probe}, M_{ref}$ in the detector plane and contain also the oscillatory dependence on the path length difference of the interferometer. We separate explicitly the field scattered by the atoms E_{sc} from the probe field E_{probe}, since in general it will not be in the same spatial mode and have a different phase. We can adjust the path length difference such to make the second integral in Eq. (4) vanish—this corresponds to the preparation of a large $\langle \hat{S}_x \rangle$ and a measurement of $\langle \hat{S}_y \rangle$ with the detector in the language of the quantum description. We note that for dispersive scattering in the far field, the probe wave and the scattered wave are nearly $\pm\pi/2$ out of phase (where the sign is determined by the atomic sublevel involved), so the first term in Eq. (4) will take its maximum value whenever the second term vanishes. The detector signal stems then from the interference of the reference wave with the scattered wave only. The atomic contribution and consequently the sensitivity of the measurement will thus be a monotonic function of both the coherently scattered power by the atoms and of the geometric overlap of the wave fronts of scattered wave and reference wave. Carrying out the overlap integral assuming perfect matching of the reference wave to the scattered wave, we write for the detector signal power S^2:

$$S^2 = 2\varepsilon^2 \left(\frac{\tau}{\hbar\omega}\right)^2 P_{sc} P_{ref}.$$

The noise will be limited from below by the shot noise of the detected photons [27]. We write the corresponding noise power N^2 as

$$N^2 = \frac{\varepsilon\tau}{\hbar\omega} 2P_{ref}.$$

With this we arrive at an equivalent expression for the signal-to-noise ratio or coupling strength as

$$\kappa^2 = \left(\frac{S}{N}\right)^2 = \frac{\varepsilon\tau}{\hbar\omega} P_{sc} = \varepsilon n_{ph}^{sc}. \tag{5}$$

Here the coupling strength is expressed in terms of the—admittedly artificial quantity (see Sec. V)—total coherently scattered power. We conclude that optimizing the sensitivity is equivalent to maximizing the scattering efficiency and

adapting the reference wave front to the scattered wave. Trivially the scattered power can be increased by increasing the input power to the interferometer. But here upper limits are set by saturation of the detectors and the requirement for low spontaneous emission rate. We choose therefore to perform the search for optimal shapes of the atomic samples and of the probe beam in the next section under conditions of constant probe power. Given a maximum pulse energy the detectors can withstand, the integrated spontaneous emission rate can be set to a desired value by choosing the single atom scattering cross section via the detuning. In the next section we calculate the scattering efficiency and the scattered wave front for selected geometries.

III. SCATTERING MODEL

In order to calculate the stationary diffracted field by the atomic density distribution we model the sample as an ensemble of fixed (i.e., infinitely heavy) point scatterers and make use of a Born approximation [28,29]. Assuming fixed positions we neglect Doppler and recoil shifts. Since we expect coherent diffraction to occur mainly close to the forward direction and we are interested in samples at ultralow temperatures, Doppler shifts will play a negligible role. On time scales short compared to the recoil time—the time needed for an atom to travel a distance of an optical wavelength at one recoil velocity—we can assume that spatial correlations are frozen, i.e., neglecting the recoil to the atom during scattering is valid [30]. In the first Born approximation we neglect multiple-scattering events and calculate the total scattered field as the sum of the fields scattered by independent single scatterers out of the probe field. This approach is justified as long as the contribution from all other scatterers to the local field seen by an individual scatterer is small compared to the probe field which demands, e.g., negligible absorption. This condition is also helped by destructive interference of scattered waves for the case of balanced sublevel populations in the experimental configuration introduced in the previous section. The condition of independent scatterers can only be met for not too high atomic density ($n_{at}<k^3$) otherwise resonant dipole-dipole interaction can change the single atom scattering properties appreciably.

A. Scattering integral

As the first ingredient we need the scattering amplitude f for a single atom. In our calculations we replace the p-wave scattering amplitude by an isotropic amplitude f equal in magnitude to the true forward-scattering amplitude. This assumption greatly simplifies analytic calculations and will be justified *a posteriori* by the observation that constructive interference occurs only close to the forward direction. Integrating $|f|^2$ over the solid angle renders the scattering cross section at a given detuning Δ of the probe laser from the atomic resonance [31]. For the experimentally relevant case of alkali atoms our choice for the scattering cross section is valid for any sublevel of the ground state probed by linearly polarized light provided the detuning Δ is large compared to the excited-state hyperfine splitting:

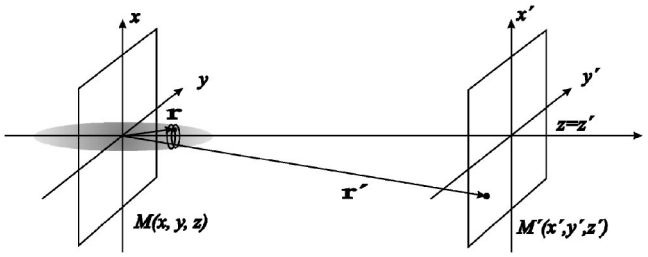

FIG. 2. Huygens-Fresnel propagation used in the model.

$$\int_{4\pi} |f|^2 d\Omega = \sigma_0 \frac{1}{1+\left(\frac{2\Delta}{\Gamma}\right)^2},$$

$$\sigma_0 = \frac{\lambda^2}{2\pi},$$

$$f = -\lambda \sqrt{\frac{3}{8\pi^2}} \frac{1+i\left(\frac{2\Delta}{\Gamma}\right)}{1+\left(\frac{2\Delta}{\Gamma}\right)^2}.$$

We remark here that this classical treatment includes the full response of the atom to the incident field, i.e., also the coupling to all empty modes of the electromagnetic field. There is no distinction between spontaneous and induced emission and the only assumption made is that the response of the atom is linear in the incident field, i.e., the atomic transition is not saturated. Naturally, since we treat the field as a classical variable, the statistical properties of the field, e.g., also the frequency spectrum of detected scattered light, are not described correctly. However, in the experimentally relevant case of large detuning and low intensity scattering is almost entirely elastic [32] and in the first Born approximation these shortcomings do not enter the problem, since exchange of photons between the atoms, i.e., multiple scattering, is neglected.

The total scattered wave is the sum of the waves scattered by individual scatterers j ($j=1\ldots N_{at}$) and can be expressed in terms of electromagnetic field vector in complex notation as (Fig. 2)

$$\vec{E}_{sc}(\vec{r}') = \sum_{j=1}^{N_{at}} \vec{E}_{probe}(r_j) f_j \frac{\exp(-ik|\vec{r}' - \vec{r}_j|)}{|\vec{r}' - \vec{r}_j|}.$$

Atoms in different internal states contribute with opposite signs to the scattered field. We thus write the weighed spatial distribution of scatterers as

$$\delta n(\vec{r}) = \sum_{k=1}^{N_2} \delta(\vec{r} - \vec{r}_k) - \sum_{l=1}^{N_1} \delta(\vec{r} - \vec{r}_l)$$

with natural normalization condition giving the population difference in the atomic sample:

$$\delta N_{at} = \int_{\mathbb{R}^3} dr^3 \delta n(\vec{r}).$$

In the following we use a continuous density distribution according to a smooth probability distribution to find a particle in a small volume element, again suitably normalized to the population difererence. This averaging procedure eliminates large-angle scattering off the microscopic density fluctuations, which is equivalent to the single-particle Rayleigh scattering background for a discrete distribution of scatterers, i.e., spontaneous emission at low saturation parameter [28]. Equally Bragg scattering of light from a regular distribution of atoms on the wavelength scale is lost by the coarse graining. The scattered field at some observation point $\vec{r}'$ outside the sample in integral form becomes

$$\vec{E}_{sc}(\vec{r}') = \int_{\mathbb{R}^2} dxdy \int_{-L}^{L} dz \vec{E}_{probe}(\vec{r}) \delta n(\vec{r}) f \frac{\exp(-ik|\vec{r}' - \vec{r}|)}{|\vec{r}' - \vec{r}|}. \tag{6}$$

In the paraxial domain (small angles to the optical axis), where we expect constructive interference of scattering amplitudes to be concentrated, we can approximate the spherical wave propagator in Eq. (6) by using a Fresnel expansion formula for the distance $|\vec{r}' - \vec{r}|$,

$$|\vec{r}' - \vec{r}| \simeq z' - z + \frac{1}{2} \frac{x'^2 + y'^2 + x^2 + y^2 - 2xx' - 2yy'}{z' - z},$$

in the phase factor, while we use $|\vec{r}' - \vec{r}| \simeq z' - z$ in the less critical denominator. Inserting this we can write the propagator in Eq. (6) as

$$K(|\vec{r}' - \vec{r}|) \simeq \frac{\exp[-ik(z' - z)]}{(z' - z)} \exp\left\{ ik \frac{xx' + yy'}{z' - z} \right\} \times \exp\left\{ -ik \frac{x^2 + y^2}{2(z' - z)} \right\} \exp\left\{ -ik \frac{x'^2 + y'^2}{2(z' - z)} \right\}.$$

Since we want to describe free diffraction of probe light and scattered light on an equal footing, we choose the incident probe beam not as a plane wave but rather as Gaussian with parameters $w(z), R(z), \Phi(z)$ being the beam radius, wavefront radius and Guoy phase, respectively,

$$\vec{E}_{probe}(x,y,z) = \vec{E}_0 \frac{w(0)}{w(z)} \exp\left\{ -i[kz - \Phi(z)] - \frac{x^2 + y^2}{w^2(z)} - ik \frac{x^2 + y^2}{2R(z)} \right\}.$$

As a realistic model for the density distribution of the trapped sample we choose a Gaussian function. This corresponds to the equilibrium shape of a thermal distribution of atoms residing inside a harmonic oscillator potential. For low enough temperature with respect to the trap depth this is a good description for a dipole trapped sample. In particular, for the transverse dimensions, where we carry out the integration of the scattering integral analytically, this choice simplifies the mathematics. We note in passing that a generalization to arbitrary transverse distributions by expansion into Hermite polynomials is possible though analytically cumbersome.

The atomic density distribution in the transverse direction has a radius w_a, which depends on z due to the weaker confinement by the dipole trap laser beam (wavelength λ_{dip}) away from its minimal beam waist. In the longitudinal direction (along the propagation axis of the probe beam) it is described by a $1/e$-length parameter L_0,

$$\delta n(x,y,z) = \frac{\delta N_{at}}{\pi^{3/2} L_0 w_a^2(z)} \exp\left(-\frac{x^2 + y^2}{w_a^2(z)} - \frac{z^2}{L_0^2} \right),$$

$$w_a(z) = w_a \sqrt{1 + \left(\frac{z}{z_{dip}} \right)^2},$$

$$z_{dip} = \frac{\pi w_a^2}{\lambda_{dip}}. \tag{7}$$

Finally, the scattered wave field can be evaluated by solving the integral

$$\vec{E}_{sc}(\vec{r}') = \int_{\mathbb{R}^2} dxdy \int_{-L}^{L} dz \vec{E}_{probe}(\vec{r}) \delta n(\vec{r}) f K(|\vec{r}' - \vec{r}|). \tag{8}$$

Here the integration over z is to be taken only over the length effectively occupied by the sample, but cannot be extended beyond the observation plane. We evaluate the scattered field distribution in some distant observation plane (M' in Fig. 2) by carrying out the integration over the transverse coordinates of the sample analytically and integrating numerically over the length of the sample. Using standard software on a desktop PC a scattered field profile can be calculated in several seconds allowing for fast interactive optimization of parameters. Not surprisingly for our model assumptions and the choice of the density distribution, we find the scattered mode profile to be very close to Gaussian in all of the studied cases and we can extract parameters like width and radius of curvature by fitting to the corresponding mode profile. The scattering efficiency is evaluated by calculating the total scattered power in the observation plane.

B. Qualitative considerations

Before presenting results of the numerical calculations some qualitative considerations are at hand to train our intuition for the results to be expected. First, the total scattered power is strictly proportional to the square of the population difference for a fixed geometry of the sample. This is a simple consequence of our continuum approximation for the density distribution and may at first sight seem disturbing, but is of course natural for coherent scattering, where constructive interference of single scattering amplitudes occurs in phase-matched directions. Second, far enough away from the sample all scattered waves will interfere constructively in the strict forward direction, so the on-axis scattered intensity for a wide probe beam will be independent of the exact geometry of the sample. This implies that scattering efficiency is determined effectively by the opening angle of the scatter-

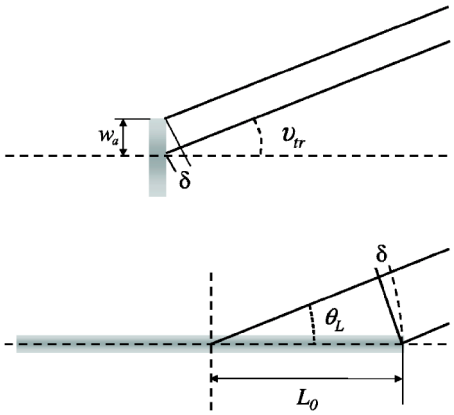

FIG. 3. Top: Diffraction limited scattering cone for Gaussian pancake-shaped sample; bottom: diffraction limited scattering cone for Gaussian pencil-shaped sample.

ing cone around the forward direction. Simple scaling arguments can be derived for this opening angle by looking at Fraunhofer diffraction from transversally and longitudinally extended samples.

Let us first look at the diffraction cone of a short homogeneous sample of width $2w_a$ (Fig. 3). To find the angle where interference of scattered waves ceases to be constructive we divide the sample in two halves. For a path length difference of half a wavelength between the ends of a half, destructive interference will occur, giving a limit to the opening angle of the scattering cone. In analogy to the far field diffraction angle of a Gaussian beam we find for a Gaussian source distribution an opening angle ν_{tr} of

$$\nu_{tr} \approx \tan\ \nu_{tr} = \frac{\lambda}{\pi w_a}. \tag{9}$$

Narrow samples scatter thus more efficiently than wide samples and integrating the angular distribution of scattered intensity predicts a $1/w_a^2$ dependence on the transverse width of the sample.

Next we consider a pencil-shaped atomic sample. For this sample $L_0 \gg w_a$. By dividing the atomic sample again into two parts (Fig. 3) we can estimate the angle at which the longitudinal extent of the cloud causes destructive interference. Introducing the path length difference δ, using a small-angle approximation and taking into account the Gaussian apodization we can estimate the opening angle θ_L as follows:

$$\delta = L_0(1 - \cos\ \theta_L) \approx L_0 \frac{\theta_L^2}{2} = \frac{\lambda}{2\pi},$$

$$\theta_L = \left(\frac{\lambda}{\pi L_0}\right)^{1/2}. \tag{10}$$

Equating the two expressions for the opening angle we can define a characteristic length z_{ra}, the atomic Rayleigh range, to compare the influence of the transverse and the longitudinal extent:

$$z_{ra} = \frac{\pi w_a^2}{\lambda}. \tag{11}$$

For atomic samples of length L_0 comparable or longer than z_{ra}, scattered waves from different sections along the propagation direction will be mismatched in phase and the total scattering cross section will be significantly reduced with respect to a short sample with the same number of atoms.

We can construct an approximate expression for the total scattered power combining the above arguments in order to cast the influence of the experimental parameters sample width, sample length, and beam diameter into a compact formula. Neglecting for a moment the change of transverse spread over the length of the sample, the scattered intensity on the optical axis far away from the sample where all atoms are phase matched is approximately

$$I_{sc}(0,0,z') \simeq \frac{3\sigma(\delta N_{at})^2}{4\pi z'^2} \frac{2P_{probe}}{\pi} \frac{w_0^2}{(w_a^2 + w_0^2)^2}, \tag{12}$$

as can be verified easily by integration of Eq. (8) in the appropriate limit. To find the total scattered power we replace the integration over the solid angle by a multiplication with $(\pi/2)\theta_{eff}^2$, where the effective opening angle θ_{eff} is chosen with the help of the Fraunhofer diffraction considerations from above. The extra factor of $1/2$ takes care of the very close to Gaussian profile of the scattered wave. We expect this to be an excellent approximation whenever the scattering cone is narrow. In order to model the tradeoff between transversal and longitudinal limitation we have to design a function which takes the value of the smaller of the two angles whenever they are grossly different. We take

$$\theta_{eff} = \left(\frac{\theta_T^2 \theta_L^2}{(\theta_T^4 + \theta_L^4)^{1/2}}\right)^{1/2}$$

with

$$\theta_T^2 = \frac{\lambda^2(w_a^2 + w_0^2)}{\pi^2 w_0^2 w_a^2}. \tag{13}$$

Here the transverse limit angle takes into account diffraction both due to the sample width as well as due to the probe beam width. There is a great deal of freedom in the choice of θ_{eff} and different definitions will lead to different functional dependencies of the scattering efficiency on the length of the sample. Our specific choice for θ_{eff} is motivated by the crossover we observe in our numerical calculations for wide probe beams presented below. Inserting the above formula we arrive after some straightforward algebra at a compact expression for the scattered power as

$$P_{sc} \simeq P_{probe}(\delta N_{at})^2 \frac{3\sigma\lambda^2}{4\pi^3 w_0^2 w_a^2} \frac{1}{1 + w_a^2/w_0^2} \frac{1}{\sqrt{1 + (L_0/\tilde{z}_{ra})^2}}. \tag{14}$$

Here we introduced $\tilde{z}_{ra}$, the modified atomic Rayleigh range, by using the definition of θ_T from Eq. (13) and the relation $\tilde{z}_{ra} = \lambda/(\pi\theta_T^2)$.

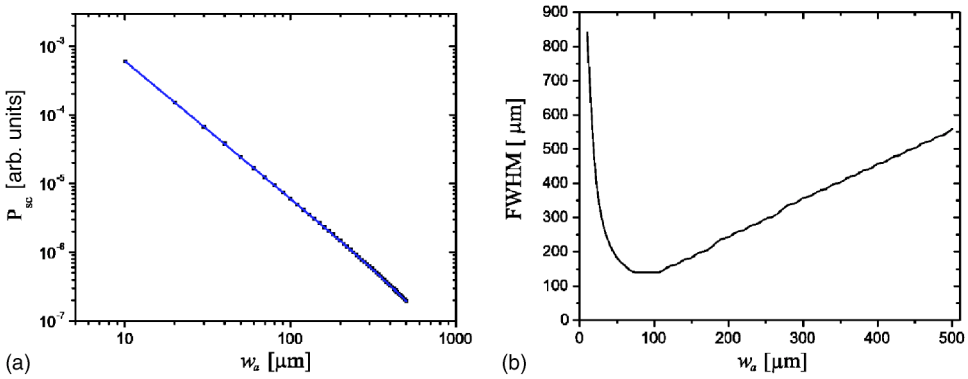

FIG. 4. (Color online) (a) Power of the scattered wave (symbols) vs the characteristic transverse radius of atomic sample of length $L_0=1$ μm for constant number of atoms and a wide probe beam $w_0=1000$ μm together with the analytic prediction from Eq. (14) (solid line). (b) Full width at half maximum of the intensity distribution in the observation plane for the same parameters.

C. Numerical solutions of the diffraction integral

Armed with the intuitive arguments and Eq. (14) for the scattering efficiency we can now proceed to present some of our numerical results. We choose parameters for the D_2 line of atomic Cs in our calculations ($\lambda=852$ nm) and keep probe power, detuning and number of atoms fixed for all results presented in this section. Figure 4(a) shows the total scattered power in the observation plane for short samples of varying transverse size.

The samples are probed by a wide ($w_0=1000$ μm) probe beam. The scattering efficiency drops dramatically with increasing sample size as expected. A comparison with the $(1/w_a^2)[1/(w_a^2+w_0^2)]$ dependence from our analytical estimate shows perfect agreement. The full width at half maximum (FWHM) of the intensity distribution in the observation plane [Fig. 4(b)] reflects the interplay of source size and diffraction in the propagation of the scattered wave. In fact, our observation plane is not located in the true far field for all source sizes and the observed dependence is equivalent to the behavior of the spread of varying size Gaussian beams at a fixed finite distance from their minimum waist position.

We investigate now how the scattered power changes with the length of the sample. In Fig. 5(a) we show the result for a narrow sample probed by a wide beam together with the analytical prediction as a function of sample length in units of z_{ra}. The rather good agreement with the simple function was our motivation to design the expression for θ_{eff} accordingly. We define the geometric factor g_L as the function describing the length dependence:

$$g_L = P_{sc}(L_0)/P_{sc}(0) \simeq \frac{1}{\sqrt{1+(L_0/\tilde{z}_{ra})^2}}. \tag{15}$$

In Fig. 5(b) we repeat the calculation over a larger range of scaled length for various transverse sizes of the sample for wide [open squares in Fig. 5(b)] and narrow [open circles in Fig. 5(b)] probe beam. The length of atomic sample is scaled here in units of $\tilde{z}_{ra}$ and the scattered power is normalized to its value at infinitesimally short sample length.

The estimate with our simple analytical formula is reasonable also over this larger range showing quantitative agreement at the level of 20% for scaled sample length up to $(L_0/\tilde{z}_{ra})=8$. The fact that scaled data for a large probe beam diameter agree among each other much better than with data from a small beam diameter is understandable from the way Eq. (14) was derived, i.e., neglecting explicitly the change of the probe beam geometry over the length of the sample. To understand the effects of changing probe geometry we consider the sample cut into thin slices. We can identify each slice as a source for a Gaussian beam wavelet, which initially

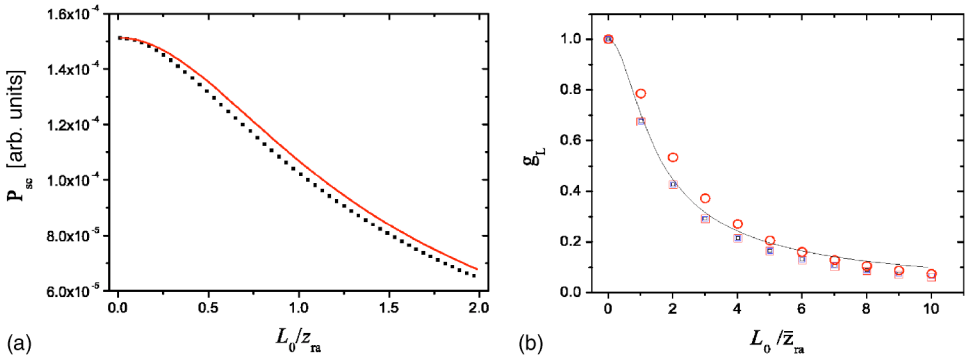

FIG. 5. (Color online) (a) Scattered power vs the characteristic length of the atomic sample with atomic waist radius $w_a=20$ μm probed by a beam $w_0=1000$ μm. Numerical data (symbols) and analytic prediction from Eq. (14) (solid line) are shown together. (b) Same as in (a) for sample width $w_a=3,5,10,20$ μm (squares) and for a narrow probe beam $w_0=w_a=20$ μm (circles) with the length scaled to $\tilde{z}_{ra}$.

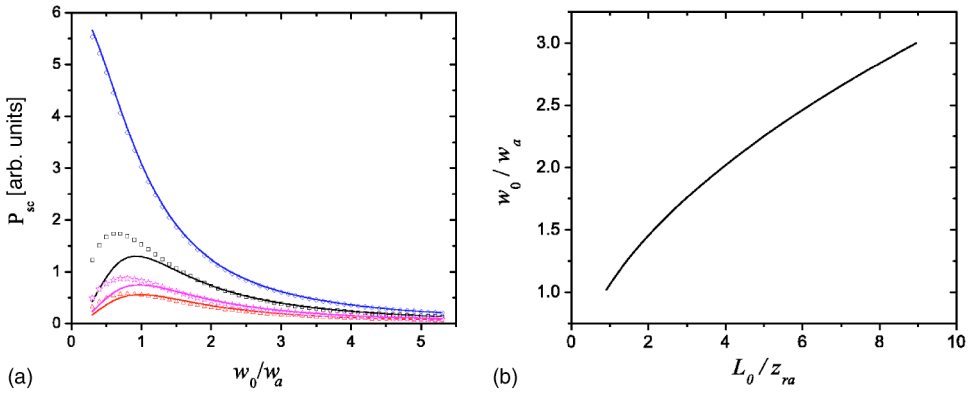

FIG. 6. (Color online) (a) Scattered power vs relative size of sample and probe beam for samples (w_a=10 μm) of length L_0=1,400,738,1000 μm (diamonds, squares, stars, triangles) together with the analytic prediction from Eq. (14) (solid lines) in scaled units; (b) predicted probe beam size to match input and scattered wave as a function of sample length in scaled units.

inherits the phase profile of the probe beam and develops wave-front curvature upon propagation. Scattered wave fronts from the back end and the front end of the sample will thus have different curvature limiting the overlap to small angles around the forward direction. Our analytic formula works well for a plane probe wave front, but fails to take into account the positive effect of a focused probe beam, which imprints wave-front curvature of the right sign to enhance wave-front overlap. For this reason the scaled scattering efficiency is slightly higher for narrow probe beams and intermediate sample length than the model predicts. For very elongated samples we see a systematic deviation of the analytical model from the numerical result and going to extremely elongated geometries we observe a different power law of the decay than suggested by the simple analytic model (see the Appendix). We refrain here from further tuning of the analytic model, since this limiting case is of little interest for coupling *all* atoms of a realistic sample efficiently to the light field and accurate quantitative data can be obtained easily numerically whenever needed, anyway.

The third important parameter which can be varied in a real experiment is the probe beam size. A probe beam size very much larger than the sample size will not be optimum. While the sample is illuminated homogeneously the field strength experienced by the atoms is rather low. The dependence with decreasing probe diameter predicted by Eq. (14) is the result of a subtle interplay of increased single atom scattering at higher intensities, increased coherent scattering efficiency for the subset of atoms which is inside the volume covered by the probe beam and decrease of the number of scatterers contributing effectively to the scattered field. In Fig. 6(a) we show the scattered power as a function of probe beam size for various sample length. Again we find that the transverse probe beam size dependence is described very well by the analytic formula for the case of a short sample. For short samples it is advantageous to use a probe beam size as small as possible. For longer samples both the numerical calculation as well as the analytical estimate predict a finite probe beam diameter for optimum scattering efficiency. For reasons already discussed in the context of Fig. 5(b) the analytical estimate starts to deviate from the numerical result for probe diameters comparable or less than the sample diameter, but works very well already for ratios as small as 2. We separate the trivial dependence on probe intensity and degree of transverse localization ($\propto w_0^{-2} w_a^{-2}$) from the observed behavior and define a geometric factor g_T describing the influence of the ratio of beam size to sample size w_0/w_a on the sample scattering efficiency as

$$g_T = \frac{1}{1 + w_a^2/w_0^2}. \tag{16}$$

For the polarization interferometric setup in Fig. 1(b) it is not possible to adapt the reference wave front to the scattered wave front separately, so instead of maximizing the scattering efficiency only, one needs to choose the input beam size such that the scattered mode has also good overlap with the input mode. For short samples it is easy to see that this can be achieved only with a probe size much smaller than the sample width, since in this limit the probe traverses a homogeneous region of the sample. For longer samples the scattering cone narrows and one can achieve good overlap also for a probe size comparable to the sample width. Equating the far-field diffraction angle of the input beam with the effective diffraction angle for light scattered off the sample, we can derive an expression for the sample length which approximately matches input and output modes:

$$\left(\frac{L_0}{z_{ra}}\right)^2 = \left(\frac{w_0}{w_a}\right)^4 \frac{\left[1 + \left(\frac{w_0}{w_a}\right)^2\right]^2 - 1}{\left[1 + \left(\frac{w_0}{w_a}\right)^2\right]^2}. \tag{17}$$

The interesting region for the ratio w_0/w_a is values bigger than 1, i.e., probe sizes comparable or bigger than the sample size. The predictions of the above equation are shown graphically in Fig. 6(b). The values obtained from the analytical formula provide good starting values for a numerical optimization of this mode-matching problem.

With our numerical calculations we explored the range of validity of a simple analytical estimate for the scattering efficiency from samples of different size and found quantitative agreement at the 20% level over a large range of parameters.

IV. APPLICATION TO A DIPOLE TRAPPED SAMPLE

The formula and numerical calculation suggest that a global optimum for the scattering efficiency exists for any sample, which simply consists in placing all scatterers in one point in space. This optimum is, alas, unphysical, because dipole-dipole interaction in that case dominates the scattering

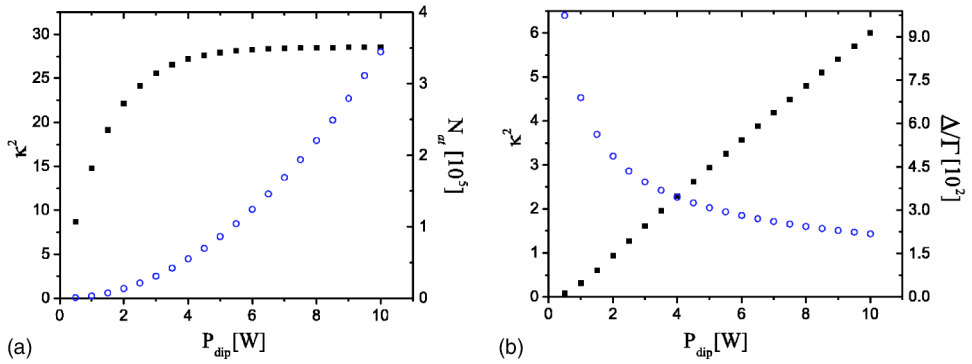

FIG. 7. (Color online) (a) achievable coupling strength (filled symbols, left axis) and number of trapped atoms (open symbols, right axis) as a function of invested dipole trap power; (b) achievable coupling strength (filled symbols, left axis) and probe detuning (open symbols, right axis) needed to satisfy $\eta = 0.1$ (see text for details).

physics and, more pragmatically, a trapped sample is subject to density limitations because of collision induced heating and losses. In the following we study the case of atoms trapped in a single Gaussian beam dipole trap. In thermal equilibrium the shape of the atomic sample in a single beam dipole trap is determined by the focal parameter of the beam [33,34]. We take parameters for Cs atoms trapped by laser radiation at $\lambda_{dip}=1030$ nm at a constant trap depth of $U_0 = k_B \times 1$ mK and fixed sample temperature of $T=100$ μK. Specifying the dipole trap laser power determines then the focal parameter needed to achieve the trap depth, and thus also the thermal radius w_a and length L_0 of the sample. Limiting the peak density to $n_{peak}=10^{12}$ cm^{-3} specifies then the number of atoms N_{at}. From Fig. 6(a) we infer that for long samples a probe beam size equal to the sample size will be close to optimum and choose this for the calculation. Restoring all prefactors and choosing a number of incident probe photons $n_{ph}=10^8$ at a detuning $\Delta/\Gamma=100$ we can then numerically determine the achievable signal-to-noise ratio (SNR) according to Eq. (5) at unity quantum efficiency as a function of the power of the dipole trap laser. In Fig. 7(a) we show the achievable SNR in this configuration, together with the number of trapped atoms. We observe that for bigger samples the SNR approaches a constant value. With the constraints we placed on temperature and density, the benefit of having more atoms is reduced by the increasingly unfavorable elongated geometry. It turns out that while the aspect ratio of the sample increases with increasing size of the dipole trap, the scaled length and hence the Fresnel number, remains constant at $\tilde{z}_{ra}/L_0 = 1/14$ [35]. With this observation, the higher number of atoms is outweighed exactly by the increasing transverse dimensions of sample and probe beam.

A realistic model for coherent light-atom coupling efficiency will have to take into account also the losses due to spontaneous emission. In fact, a measurement on atoms with a spontaneous emission probability approaching 1 can hardly be considered nondestructive for the collective variable. The result from the 1D quantum model in Eq. (2) predicts actually that the achievable SNR and the level of destructiveness are coupled, i.e., the achievable SNR is directly proportional to the integrated single atom spontaneous emission rate η (see also Refs. [36,37]). Since the transverse size of the trapped sample changes with the invested dipole trap power, η is not the same for the data points in Fig. 7(a). In order to make a fair comparison we thus calculate for each of the data points the number of spontaneously emitted photons per atom by evaluating the average intensity experienced by the atoms and integrating over the pulse time (see Appendix, Sec. II). In Fig. 7(b) we show the same data rescaled to a probe laser detuning, such that $\eta=0.1$ for every point, together with the detuning needed to satisfy the constraint on η.

Including the condition of equal level of destructiveness restores the advantage of bigger samples over small samples. We note that the absolute numbers for the coupling strength at fixed η cannot be changed by simultaneous variation of the detuning and the number of incident photons, since the coupling strength and η depend in the same way on these two quantities. For the elongated samples probed by a narrow beam the losses are distributed quite unevenly over the sample due to the rather inhomogeneous illumination.

V. RELATION TO EFFECTIVE 1D MODELS

At the start of our scattering calculation we expressed the coupling strength or achievable SNR in terms of a number of coherently scattered photons. This number, although convenient to calculate, is not a directly measurable quantity, since we cannot distinguish coherently scattered photons from the incident photons in principle and only their interference is observable. The results from the previous sections allow us to express this artificial scattered power in terms of the incident power and the interaction geometry. This also makes a direct comparison to the expression for the coupling strength derived from the 1D quantum model possible. Introducing the transverse beam area A_{ph} as πw_0^2 and equivalently the sample area A_{at} as πw_a^2 we rewrite Eq. (14) in the limit of large detuning as [38]

$$P_{sc} = \frac{3}{2}(\delta N_{at})^2 \frac{\sigma_0}{A_{ph}} \frac{\sigma_0}{A_{at}} \left(\frac{\Gamma}{2\Delta}\right)^2 g_T g_L P_{inc}.$$

Using Eq. (5) and $\langle \delta N_{at}^2 \rangle = N_{at}/2$ [39] we obtain the SNR assuming unit quantum efficiency detection as

$$\kappa^2 = \left(\frac{S}{N}\right)^2 = g_T g_L \frac{3\sigma_0^2}{A_{at} A_{ph}} N_{at} n_{ph} \left(\frac{\Gamma}{2\Delta}\right)^2. \tag{18}$$

Comparing this to the expression obtained from an effective 1D model in Sec. II, viz. Eq. (2),

$$\kappa^2 = \frac{\sigma_0^2}{A^2} N_{at} n_{ph} \left(\frac{\Gamma}{2\Delta}\right)^2, \tag{19}$$

we see how diffraction effects modify the coupling strength with respect to the predictions from the 1D model. The two

expressions give the same values for the case of a sample with effective Fresnel number close to 1 and equal probe and sample diameter [40]. For our choice of Gaussian sample and probe the modification of coupling strength can be quantitatively accounted for by the geometrical factors. We believe that the asymptotic scaling of the geometrical factors will be independent of the specific choice of the function describing the shape of the sample. We can look at the case of a very elongated sample ($L_0 \gg \tilde{z}_{ra}$) probed by a narrow beam of the same size as the sample by expanding the geometric factors accordingly and find in this limit for the coupling strength,

$$\kappa^2 = \frac{\pi^{3/2}}{8}\left(\frac{\lambda}{2\pi}\right)^3 n_{peak} n_{ph}\left(\frac{\Gamma}{2\Delta}\right)^2. \tag{20}$$

The achievable coupling strength becomes independent of the sample size in this limit and is linear in the peak atomic density n_{peak}, instead of being proportional to column density as in the 1D model [41]. The numerically observed scaling with the length of the sample (see the Appendix) reduces the coupling even more for extremely elongated samples.

VI. CONCLUSION

In this paper we have outlined an efficient method to include diffraction effects in the coupling of light to collective variables of atomic samples and applied it to an experimentally relevant case of atomic ensembles stored in single beam dipole traps. The use of Gaussian light fields is well adapted to real experimental geometries and allows for a largely analytical treatment. Tayloring the sample and beam geometry, such that probe mode and scattered mode coincide is possible and will be useful for polarization interferometry or multipass experiments.

Several approximations have been made, mainly to keep the model as transparent as possible, and some of them can be lifted in future extensions of the model. The leading-order effect of multiple scattering and particle statistics on the refractive index, which we are effectively calculating in a single scattering approximation, can be accounted for by a correction term depending on the local density of scatterers which will allow us to calculate the geometry of the scattered mode also for higher densities [42].

Our model is classical in nature, but the point scatterer model can be used also to analyze quantum noise contributions and their dependence on geometry. Giving up the continuous density distribution one can determine numerically the scattering efficiency from randomly distributed samples and this way statistically analyze the noise introduced onto the scattered wave front by density fluctuations on different length scales. This models spontaneous emission noise as well as nontrivial effects like the inherent mode-matching noise discussed in Ref. [13]. There are already studies using a wave function Monte Carlo technique to address the effects of spontaneous emission in a quantum description [43] adapted for our case of trapped inhomogeneous samples, but the extremely fast increase of the dimensionality of Hilbert space limits the treatment to very small numbers of atoms only. A classical point scatterer calculation can be used conveniently also to model experimental imperfections, e.g., alignment errors, where the analytical integration over the transverse distribution would become much more involved.

The assumption of infinitely heavy scatterers, i.e., the neglect of photon recoil, needs closer attention, when the fluctuations of collective variables are studied. In fact, when working with collective atomic variables one usually assumes that internal and external degrees of freedom of the atomic sample are decoupled. Already without multiple scattering the change of momentum due to scattering introduces correlations between internal and external variables [44]. Also, a focused probe beam with inhomogeneous intensity distribution across the sample exerts a dipole force on the sample leading to contraction or expansion depending on the sublevel populations for the setup in Fig. 1(a). This leads to an effective decay mechanism for the macroscopic coherence between the sublevels. Similar effects occur naturally also at the level of quantum fluctuations. Ultimately, a proper quantum model will have to take into account the scattering induced dynamics of the density correlation function of the sample, which determines the structure factor for light scattering [45,46]. Prominent examples for the key importance of the photon recoil for collective scattering are the observation of super-radiant Rayleigh and Raman scattering in Bose-Einstein condensates [47,48], cavity cooling [49,50], and collective motion in high-finesse cavities [51].

ACKNOWLEDGMENTS

J.H.M. thanks K. Mølmer and A. Sørensen for stimulating discussions. We acknowledge support for this work by the EU-network CAUAC and Dansk Grundforskningsfond.

APPENDIX

1. Improved geometrical factor g_L

The analytical estimate for the total scattered power given in Eq. (14) is seen to fail for very elongated samples. This can be traced back to the assumption of homogeneous illumination in the calculation of the on-axis intensity of the scattered field. A simple way to arrive at an improved estimate is to introduce an axial average of the incident intensity in order to take into account the diffractive spreading of the incident beam over the sample length. Since the scattering efficiency depends quadratically on atom number, the average is performed over the squared density distribution and to simplify the math the Gaussian atomic density distribution is replaced by a rectangular distribution of same peak height and area:

$$I_{eff} = \frac{I_0}{\sqrt{\pi/2}L_0}\int_0^{\sqrt{\pi/2}L_0} \frac{1}{1+(z/z_r)^2}dz$$

$$= I_0 \frac{z_r}{\sqrt{\pi/2}L_0}\arctan(\sqrt{\pi/2}L_0 z_r^{-1}). \tag{A1}$$

Here $z_r = \pi w_0^2/\lambda$ denotes the Rayleigh range of the laser beam. The inhomogeneous axial illumination changes also

the effective length of the sample entering the estimate for the opening angle of the diffraction cone. Incorporating this effect we find empirically an improved expression for the longitudinal geometrical factor [see Eq. (15)],

$$g_L' = \left(\frac{2}{\pi}\frac{z_r^2}{L_0^2}\right)^{1/2} \arctan\left\{\frac{\pi}{2}\frac{L_0^2}{z_r^2}\frac{1+(L_0\tilde{z}_{ra}z_r^{-2})^2}{1+(L_0\tilde{z}_{ra}^{-1})^2}\right\}^{1/2} \times[1+(L_0\tilde{z}_{ra}z_r^{-2})^2]^{-1/2} \quad \text{(A2)}$$

which fits our numerical data at the level of 20% for Fresnel numbers of the atomic sample up to 1/80.

2. Spontaneous emission rate

Within the framework of the point scatterer model the distinction between spontaneous and induced emission is blurred and with the approximation of a microscopically continuous density distribution for the point scatterers spontaneous emission is completely lost. Introducing implicitly microscopic density fluctuations and assuming that single atom spontaneous emission happens independently of the presence of the neighboring scatterers the spontaneously emitted power per atom can be calculated as

$$\frac{\eta}{\tau} = \left\langle \frac{P_{spon}}{\hbar\omega N_{at}} \right\rangle = \frac{\sigma}{\hbar\omega}\int_{\mathbb{R}^3} I_{inc}(\vec{r})n(\vec{r})dV. \quad \text{(A3)}$$

Setting for simplicity the wavelength of the dipole trap laser, which determines the change in transverse dimensions of the atomic sample, equal to the wavelength of the incident radiation, the single atom spontaneous emission rate can be written in the form

$$\frac{\eta}{\tau} = \frac{\sigma}{\hbar\omega}\frac{2P_{probe}}{\pi w_0^2}[1+2(w_a/w_0)^2]^{-1}\pi^{-1/2}\int_{-\infty}^{\infty}\frac{\exp(-z^2)}{1+(z/a)^2}dz,$$

with

$$a = \frac{z_r}{L_0}\left(\frac{1+2(w_a/w_0)^2}{3}\right)^{1/2}$$

and

$$\int_{-\infty}^{\infty}\frac{1}{1+(z/a)^2}\exp(-z^2)dz = a\pi\,\exp(a^2)\mathrm{Erfc}(a)$$

where $\mathrm{Erfc}(a)$ denotes the complementary error function.

The separation of the expression for the coupling strength κ^2 into integrated spontaneous emission η and an effective optical depth α as in the 1D description can be done in principle, but does not lead to simple analytical expressions. In fact, such a separation is also not very meaningful when done globally, since the time-integrated spontaneous emission rate can have substantial *local* variations due to the inhomogeneous illumination. In addition, the contribution of a central volume element to the total scattered field and thus to the scattering efficiency is much bigger than for a volume element on the rim of the density distribution. This means that a spontaneous emission or optical pumping event in the center of the sample leads to a more pronounced change in the scattering efficiency. In a quantum description the spatial inhomogeneity of both light and atom variables naturally suggests importance sampling and leads to a concept of collective variables which are no longer fully symmetric with respect to exchange of single-particle labels [14].

[1] A. Kuzmich, K. Mølmer, and E. S. Polzik, Phys. Rev. Lett. **79**, 4782 (1997).

[2] A. Kuzmich, N. P. Bigelow, and L. Mandel, Europhys. Lett. **42**, 481 (1998).

[3] L. M. Duan, J. I. Cirac, P. Zoller, and E. S. Polzik, Phys. Rev. Lett. **85**, 5643 (2000).

[4] A. Kuzmich and E. S. Polzik, Phys. Rev. Lett. **85**, 5639 (2000).

[5] A. E. Kozhekin, K. Mølmer, and E. Polzik, Phys. Rev. A **62**, 033809 (2000).

[6] L. K. Thomsen, S. Mancini, and H. M. Wiseman, Phys. Rev. A **65**, 061801 (2002).

[7] B. Kraus, K. Hammerer, G. Giedke, and J. I. Cirac, Phys. Rev. A **67**, 042314 (2003).

[8] J. Fiurášek, Phys. Rev. A **68**, 022304 (2003).

[9] J. Hald, J. L. Sørensen, C. Schori, and E. S. Polzik, Phys. Rev. Lett. **83**, 1319 (1999).

[10] A. Kuzmich, N. P. Bigelow, and P. Mandel, Phys. Rev. Lett. **85**, 1594 (2000).

[11] B. Julsgaard, A. Kozhekin, and E. S. Polzik, Nature (London) **413**, 400 (2001).

[12] C. Schori, B. Julsgaard, J. L. Sørensen, and E. S. Polzik, Phys. Rev. Lett. **89**, 057903 (2002).

[13] L. M. Duan, J. I. Cirac, and P. Zoller, Phys. Rev. A **66**, 023818 (2002).

[14] A. Kuzmich and T. A. B. Kennedy, Phys. Rev. Lett. **92**, 030407 (2004).

[15] W. Happer and B. S. Mathur, Phys. Rev. Lett. **18**, 577 (1967).

[16] A. Kuzmich, L. Mandel, J. Janis, Y. E. Young, R. Ejnisman, and N. P. Bigelow, Phys. Rev. A **60**, 2346 (1999).

[17] In writing this Hamiltonian we drop terms which depend on the total number of atoms and photons and are unimportant for the dynamics.

[18] Strictly speaking the operators contain the retarded Fourier transforms of the (cross) spectral densities of the electric field components. For a more rigorous treatment of the propagating field modes we refer to Ref. [3].

[19] Spatial correlations due to the indistinguishability of the particles are neglected here.

[20] This procedure is valid for Gaussian input states like coherent or squeezed states.

[21] A. Sinatra, J. F. Roch, K. Vigneron, P. Grelu, J.-P. Poizat, K. Wang, and P. Grangier, Phys. Rev. A **57**, 2980 (1998).

[22] K. Hammerer, K. Mølmer, E. S. Polzik, and J. I. Cirac, Phys. Rev. A **70**, 044304 (2004).

[23] D. J. Wineland, J. J. Bollinger, W. M. Itano, and D. J. Heinzen, Phys. Rev. A **50**, 67 (1994).
[24] B. Julsgaard, J. Sherson, J. I. Cirac, J. Fiurášek, and E. S. Polzik, Nature (London) **432**, 482 (2004).
[25] A. Kuzmich and E. S. Polzik, in *Quantum Information with Continuous Variables*, edited by S. L. Braunstein and A. K. Patel (Kluwer Academic Publishers, Dordrecht, 2003), pp. 231–265.
[26] D. Oblak, J. K. Mikkelsen, W. Tittel, A. K. Vershovski, J. L. Sørensen, P. G. Petrov, C. L. Garrido Alzar, and E. S. Polzik, e-print quant-ph/0312165, Phys. Rev. A (to be published).
[27] Here we reintroduce implicitly the noise due to quantum fluctuations.
[28] P. de Vries, D. V. van Coevorden, and A. Lagendijk, Rev. Mod. Phys. **70**, 447 (1998).
[29] M. Born and E. Wolf, *Principles of Optics*, 7th ed. (Cambridge University Press, Cambridge, England, 1999), Chap. XIII.
[30] For Cs atoms probed on the D_2 line the recoil time is 0.3 ms.
[31] Since we treat the scattered wave as a scalar the phase of the scattering amplitude has to be chosen with care.
[32] B. R. Mollow, Phys. Rev. A **12**, 1919 (1975).
[33] R. Grimm, M. Weidemüller, and Y. B. Ovchinnikov, Adv. At., Mol., Opt. Phys. **42**, 95 (2000).
[34] Here we neglect other potentials, like gravity, for simplicity.
[35] Our simple analytical estimate at this length is already wrong by about a factor of 2.
[36] G. Smith, S. Chaudhury, and P. S. Jessen, J. Opt. B: Quantum Semiclassical Opt. **5**, 323 (2003).
[37] J. E. Lye, J. J. Hope, and J. D. Close, Phys. Rev. A **67**, 043609 (2003).
[38] The scattering cross section as an atomic property enters our calculation only once, consequently $\Gamma^2/4\Delta^2$ appears linearly here.
[39] This value corresponds to the variance in the population difference for a sample of N_{at} independent atoms residing with equal probability in two internal states.
[40] M. G. Raymer and J. Mostowski, Phys. Rev. A **24**, 1980 (1981).
[41] The density in units of $(\lambda/2\pi)^3$ has to be smaller than 1 for the model to be valid, otherwise the neglect of multiple scattering is not possible.
[42] O. Morice, Y. Castin, and J. Dalibard, Phys. Rev. A **51**, 3896 (1995).
[43] I. Bouchoule and K. Mølmer, Phys. Rev. A **66**, 043811 (2002).
[44] A. V. Rau, J. A. Dunningham, and K. Burnett, Science **301**, 1081 (2003).
[45] To lowest order in a multiple-scattering expansion the dynamics of the density correlation function can be just described by recoil heating.
[46] H. D. Politzer, Phys. Rev. A **55**, 1140 (1997).
[47] S. Inouye, A. Chikkatur, D. Stamper-Kurn, J. Stenger, D. Pritchard, and W. Ketterle, Science **285**, 571 (1999).
[48] D. Schneble, G. K. Campbell, E. W. Streed, M. Boyd, D. E. Pritchard, and W. Ketterle, Phys. Rev. A **69**, 041601 (2004).
[49] P. Horak, G. Hechenblaikner, K. M. Gheri, H. Stecher, and H. Ritsch, Phys. Rev. Lett. **79**, 4974 (1997).
[50] V. Vuletic and S. Chu, Phys. Rev. Lett. **84**, 3787 (2000).
[51] B. Nagorny, T. Elsässer, and A. Hemmerich, Phys. Rev. Lett. **91**, 153003 (2003).